




# Influence of Au plasmons and their synergistic effects with ZnO nanorods for photoelectrochemical water splitting applications

Sayed Abdul Saboor<sup>1</sup>, Vidhika Sharma<sup>1</sup>, Ebrima L. Darboe<sup>1</sup>, Vidya Doiphode<sup>1</sup>, Ashvini Punde<sup>1</sup>, Pratibha Shinde<sup>1</sup>, Vijaya Jadkar<sup>1</sup>, Yogesh Hase<sup>1</sup>, Ashish Waghmare<sup>1</sup>, Mohit Prasad<sup>1,\*</sup>, and Sandesh Jadkar<sup>2,\*</sup> 

<sup>1</sup>School of Energy Studies, Savitribai Phule Pune University, Pune 411 007, India

<sup>2</sup>Department of Physics, Savitribai Phule Pune University, Pune 411 007, India

**Received:** 13 February 2021

**Accepted:** 4 July 2021

**Published online:**

22 July 2021

© The Author(s), under exclusive licence to Springer Science+Business Media, LLC, part of Springer Nature 2021

## ABSTRACT

Herein, Au plasmons and their synergistic effects with ZnO nanorods (ZNs) have been investigated for photoelectrochemical (PEC) water splitting application. Au plasmons and ZNs are deposited electrochemically. Au-modified nanostructures have absorption in the visible region as plasmons enhance charge transfer and inhibit charge recombination. ZNs modified with Au (deposition duration  $\sim 60$  s) have a photo-current density of  $\sim 660 \mu\text{A cm}^{-2}$ , at a bias of 1.0 V/SCE. X-ray diffraction (XRD) and scanning electron microscopy were used to study the structure and surface morphology of fabricated photoanodes. In addition, UV-Visible absorption and Photoluminescence spectroscopy were used for optical characterization. We have recorded current-voltage measurements and photo-conversion efficiency measurements to substantiate our observations of the synthesized photoanodes for future application in PEC splitting of water. We have also carried out Mott-Schottky and electrochemical impedance spectroscopy analysis. The analysis reveals that Au-modified ZNs-based photoanodes are a better proposition than their bare counterparts for PEC water splitting application.

## 1 Introduction

Sustainable energy economy can be achieved by converting solar energy into chemical fuels, for which photoelectrochemical (PEC) water splitting is the most promising route. PEC splitting of water utilizes the sun's astounding potential and readily available

water to produce hydrogen [1–5]. In PEC cells, the semiconductor material is the most critical component. It should have sizeable visible spectrum absorption, straddling band edges, large lifetime of charge carriers, high carrier mobility, and must be stable and economical [6, 7]. The essential kinetic and thermodynamic conditions to realize a single

Address correspondence to E-mail: mohitprasad7@gmail.com; sandesh@physics.unipune.ac.in

semiconductor are still elusive [8]. Photoanodes based on Si and III-V semiconductors have exhibited record STH efficiency value up to 19.3%, but these materials suffer from poor stability [9]. These semiconductors satisfy a bunch of mandatory conditions, but they are associated with high manufacturing costs. However, for semiconductors, the long-term device durability is compromised due to poor stability in PEC conditions. On the other hand, earth-abundant metal oxides, such as ZnO, TiO<sub>2</sub>, WO<sub>3</sub>,  $\alpha$ -Fe<sub>2</sub>O<sub>3</sub>, and BiVO<sub>4</sub>, exhibit outstanding properties and can be viable options for PEC cells [9]. These earth-abundant metal oxides have low processing cost, high stability, low minority carrier diffusion length, high recombination, and low light absorption.

Plasmonics has emerged as a powerful tool to overcome the general drawbacks of metal oxides by integrating with photoanodes and enhancing PEC cell's performance. Plasmons have unusual optical properties. Their physical size is exceeded by absorption and scattering cross-section. A metal usually absorbs solar radiation and converts it into heat radiation, but plasmons have diverted researcher's interest to plasmon-assisted photocatalysis. Photon absorption promotes non-equilibrium carrier distribution. High-energy carriers can tunnel out of the metal into high-energy orbitals of the molecules in the vicinity, thereby catalyzing the reaction. This mechanism is known as the *hot carrier mechanism*. This mechanism retards the electron-hole recombination and improves the PEC efficiency by acting as electron trap centers [10–12]. Numerous researchers have probed the *hot electron* phenomena for PEC activity, and various configurations have been probed such as Ag/Au/TiO<sub>2</sub> [13, 14], Ag/Au/ZnO [15, 16], Au/Fe<sub>2</sub>O<sub>3</sub> [17], Au/BiVO<sub>4</sub> [18], Au/MoS<sub>2</sub> [19], Au/ZnFe<sub>2</sub>O<sub>4</sub> [20], Au/SrTiO<sub>3</sub> [21], and Au/CuO [22]. In every case, *hot electron phenomena* have helped in improving the efficiency of the PEC process. So we were motivated to pick plasmonic material in conjunction with wide band gap material for our experimental work. Au is an important plasmonic material as it exhibits a hot electron phenomenon and has a high Q-factor. Q-factor is responsible for high plasmonic strength, and Au has an inherent high Q-factor [23]. Moreover, for PEC applications, ZnO is the most studied material [23–27]. ZnO is a direct band gap material (3.2 eV) with high electron mobility and exciton binding energy. ZnO band edges straddle well with the redox

potentials, and it is reasonably stable at pH 7.0. However, ZnO has poor absorption in the visible region, its prominent drawback [28, 29]. To increase absorption in the visible region in ZnO for PEC splitting, doping is an effective strategy, but it has its limitations [30–33].

The incorporation of Au/Ag in hierarchical ZnO structures is also used to enhance the PEC activity. For example, Liu et al. [34] used Au/ZnO nanorods to enhance PEC water splitting efficiency. Ag/ZnO micro/nanoflowers are also for enhanced photocatalytic performance and antibacterial activity [35]. Wei and coworkers [36] reported the decoration of Au nanoparticles on ZnO/CdS nanotube arrays for plasmon-enhanced water splitting. Similarly, Wang et al. [37] sensitized ZnO nanopencil arrays by Au nanoparticles for PEC water splitting. Kumari and others [38] reported enhancement in PEC water splitting due to surface deposition of Au and Ag nano-isles on ZnO thin films. With this motivation, we have synthesized 1D ZnO nanorods (ZNs) thin films by electrodeposition method, a straightforward and versatile method for depositing thin films. Then Au plasmons were incorporated on ZNs through electrochemical deposition. For PEC splitting of water, the present study investigates the effect of electrodeposited Au plasmons on ZNs-based photoanodes in distinct configurations. To evaluate the structural and optical properties of Au plasmons on ZNs-based photoanodes, x-ray diffraction (XRD), scanning electron microscope (SEM), UV-Visible absorption spectroscopy, and photoluminescence (PL) analysis were carried out. In addition, current-voltage (J-V) characteristics, electrochemical impedance spectroscopy (EIS), Mott-Schottky (MS) analysis, and photo-conversion efficiency (PCE) measurements have been used to validate the obtained PEC water splitting results. We found that ZNs-Au photoanodes had enhanced photo-current ( $\sim 0.66 \text{ mA/cm}^2$ ) compared to pristine-ZNs photoanodes ( $\sim 0.32 \text{ mA/cm}^2$ ) at a bias of 1.0 V/RHE.

## 2 Materials and methods

### 2.1 Synthesis of Au-sensitized ZNs-based photoanodes

Electrochemical deposition of Au plasmons dispersed ZnO nanorods array was carried out in a

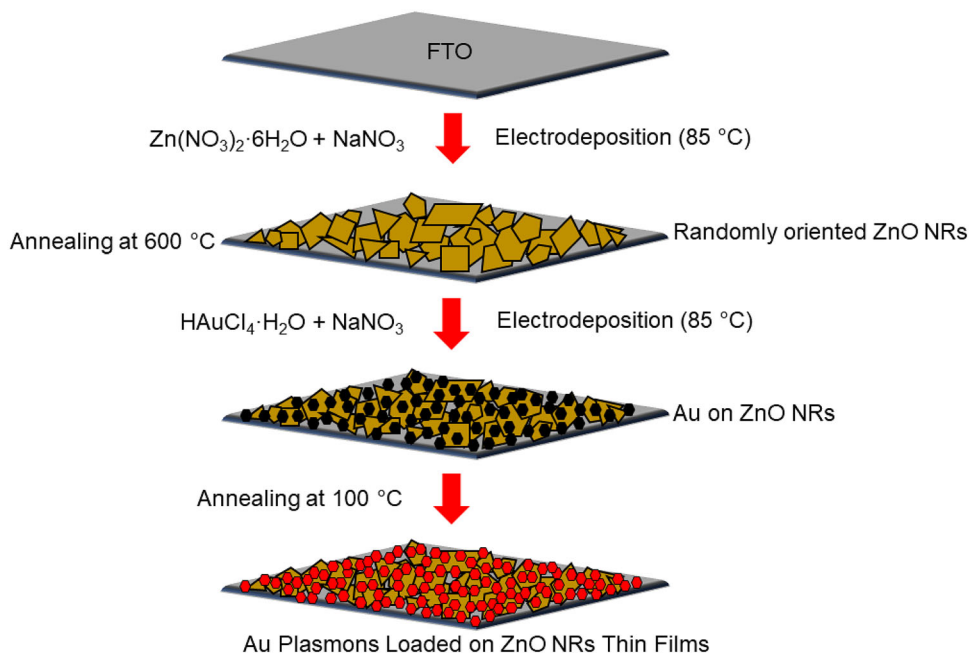
3-electrode cell. For synthesizing photoanodes, conducting glass substrate (FTO) was used. Pt mesh and Saturated calomel electrode (SCE) were used as a counter electrode and a reference electrode. Prior to deposition, FTO-coated glass substrates were cleaned using standard procedure [31]. An aqueous solution comprising 5 mM  $\text{Zn}(\text{NO}_3)_2 \cdot 6\text{H}_2\text{O}$  and a 50 mM  $\text{NaNO}_3$  electrolyte bath sustained at 85 °C was used to synthesize ZnO nanorods (ZNs). Step potentials of  $-1.3$  and  $-1.0$  V were applied for 15 and 2000s, respectively. After deposition, thin films were cleaned using deionized water and then dried. To improve the crystallinity, ZNs-based photoanodes were annealed in air at 600 °C.

Further, Au plasmons were electrochemically loaded on ZNs photoanodes. Au plasmons-loaded ZNs thin films were prepared at 30 s, 45 s, 60 s, and 75 s loading/deposition time of Au. These films are ZNs-Au 30 s, ZNs-Au 45 s, ZNs-Au 60 s, and ZNs-Au 75 s, respectively, whereas the unloaded ZNs are denoted as pristine-ZNs. After electrodeposition, all the fabricated thin films were dried at 100 °C for 1 h in the oven. Figure 1 shows the schematic for the growth mechanism of ZnO nanorods and Au plasmons loaded on ZnO nanorods thin films for different deposition durations.

## 2.2 Characterization and measurement setup

Low-angle XRD was used to determine the crystal structure of the synthesized photoanodes. Bruker D8 Advance, Germany, X-ray diffractometer equipped with  $\text{Cu-K}\alpha$  irradiation ( $\lambda = 1.54 \text{ \AA}$ ), in the range of (20–60°), was used to record the diffractograms. SEM was used to analyze the nanostructure of ZnO and also Au deposited on it. It was recorded using a SEM (JEOL JSM630A). UV–Visible spectroscopy was used to determine the film's absorption spectra, which was used to calculate the Tauc plot and bandgap energy of the given materials. It was recorded by UV-/Vis spectrophotometer (JASCO V-670). I-V characteristic was used to measure the photoconductivity of synthesized photoanodes with different concentrations of Au plasmons using the Autolab PGSTAT302N instrument under dark and illumination. MS and EIS were recorded to calculate concentration, flat band potential, and lifetime of charge carriers, respectively. PL spectroscopy was used to investigate the defects present in the synthesized photoanodes. It was recorded by (Horiba Fluorolog) spectrophotometer. The excitation wavelength was 350 nm.

**Fig. 1** Schematic for the growth mechanism of ZnO nanorods and Au plasmons loaded on ZnO nanorods thin films by electrodeposition for different deposition durations



### 3 Results and discussion

#### 3.1 Low-angle x-ray diffraction (XRD) analysis

Low-angle XRD was used to study the crystal structures, atomic spacing, and phase orientation of the synthesized photoanodes. It is based on the constructive interference of monochromatic X-ray, which is diffracted from the crystalline sample. Figure 2 shows the XRD pattern of Au plasmons loaded on ZNs for different deposition times on FTO substrate. In addition, the XRD pattern of pristine-ZNs is also shown in the XRD pattern for comparison. Hash (#) indicates the peaks due to underlying FTO substrate.

As seen, the XRD pattern of pristine-ZNs and Au plasmons loaded on ZNs for different deposition times has diffraction peaks at  $2\theta$ –31.8°, 34.4°, 36.3°, and 47.5° corresponding to the crystal planes (100), (002), (101), (102), and (110) of crystalline ZNS, respectively. All diffraction peaks could be readily indexed as hexagonal wurtzite structure for ZNs having lattice constants of  $a = b = 3.28 \text{ \AA}$  and  $c = 5.25 \text{ \AA}$ , which is in good agreement with JCPDS data card # 01-36-1451. These identified crystal planes of ZNs are consistent with the previously reported results [39]. In addition, two diffraction peaks are also observed at  $2\theta$ –38.3° and 44.5° in the XRD pattern for

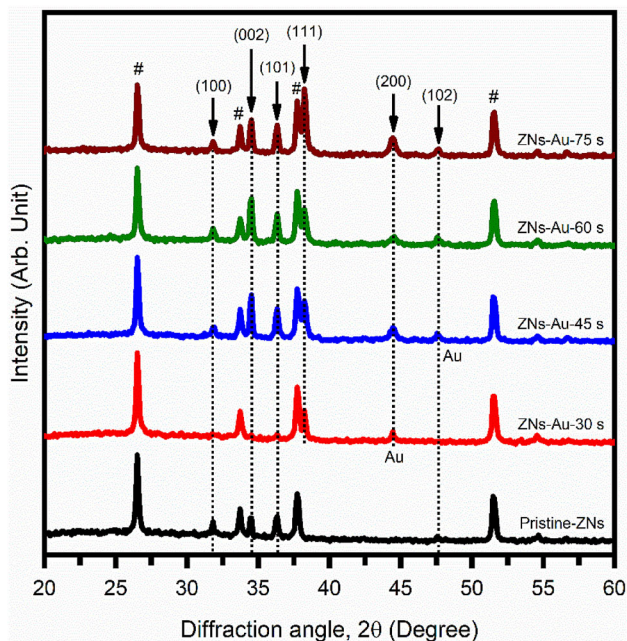


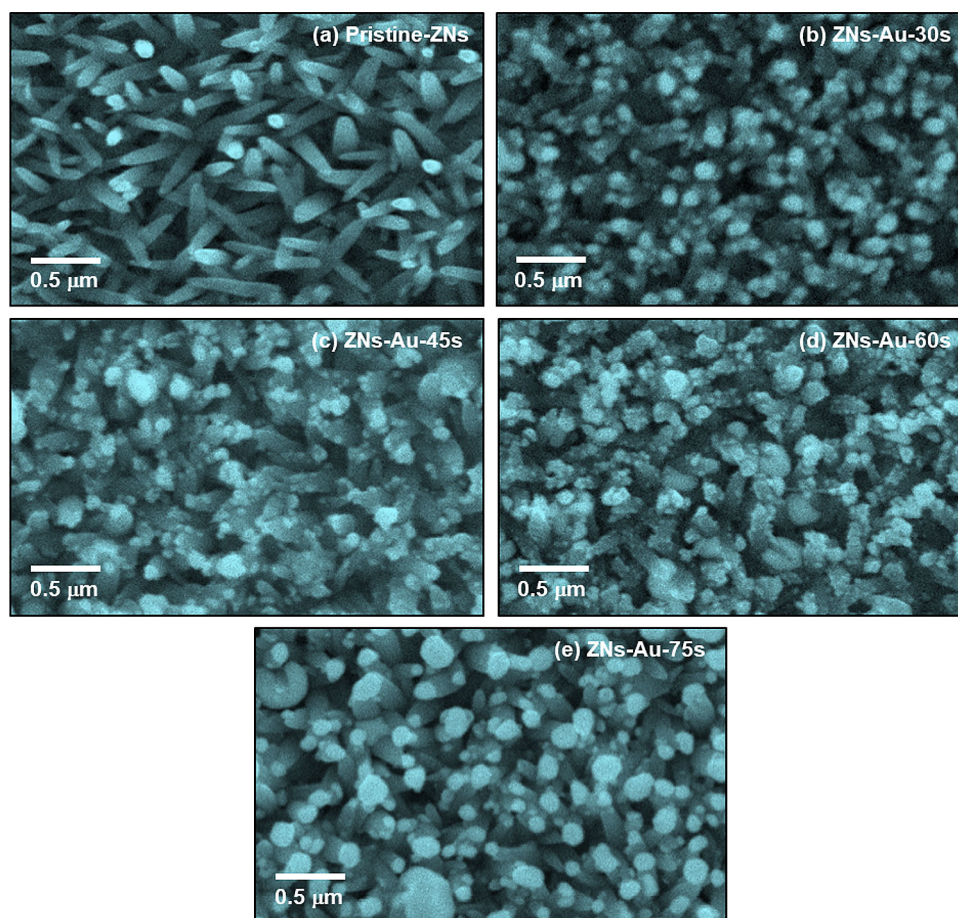
**Fig. 2** Low-angle XRD pattern of pristine-ZNs and Au plasmons loaded on ZNs for different deposition durations

ZNs deposited for different deposition times. These peaks are associated with Au plasmons deposited on ZNs. They are assigned to (111) and (200) reflection planes, respectively [40], and also indicate that the crystal structure is face-centered cubic (FCC) with the lattice constant  $4.2 \text{ \AA}$  [JCPDS data card # 04-784]. Furthermore, the intensity of peaks related to Au plasmons increases with an increase in deposition time. For instance, the peak of (111) at  $2\theta \sim 38.3^\circ$  for a deposition time of 75 s has a considerable increment in intensity than 60 s, 45 s, and 30 s. Thus, it can be linked to the presence of high crystallinity of Au plasmons. These results indicate the successful loading of Au plasmons on ZNs by electrochemical deposition.

#### 3.2 Surface morphology analysis

Scanning electron microscopy (SEM) was used to investigate the surface morphology of pristine-ZnO and Au plasmons loaded on ZnO for different deposition durations. Before imaging, the samples were coated with platinum by the sputtering method. Figure 3 shows the SEM images of pristine-ZnO and Au plasmons loaded on ZnO photoanodes for different deposition durations. The SEM micrograph of pristine-ZnO (Fig. 3a) clearly shows randomly distributed nanorods perpendicular to the substrate surface with different angles to each other and ample space between them. The length of pristine-ZnO nanorods (ZNs) is  $\sim 1.5 \mu\text{m}$ . The diameter of ZNs was estimated by using Image J software. The diameter is found approximately in the range of  $\sim 100$ – $200 \text{ nm}$ , with an average value of  $\sim 150 \text{ nm}$ . The SEM micrographs of Au plasmons loaded on ZnO for different deposition durations (Fig. 3b–e) show a salient change in the growth morphology after incorporating Au plasmons. Figure 3b–e show that the Au plasmons are uniformly distributed over ZNs. Interestingly, the ZNs maintain their vertically oriented characteristics even after incorporating Au, although the time deposition durations were different. It leads to variation in Au's distribution density and size over ZNs. The retention of nanorod morphology of ZnO after the Au incorporation is beneficial for water splitting application. Due to their one-dimensional structure, ZNs can facilitate more efficient carrier transports because of decreased grain boundaries, surface defects, disorders, and discontinuous interface.

**Fig. 3** SEM images of **a** Pristine- ZNs, **b** ZNs-Au-30 s, **c** ZNs-Au 45 s, **d** ZNs-Au 60 s, and **e** ZNs-Au 75 s photoanodes



The average diameter of Au plasmons obtained by image J software was found  $\sim 136$  nm. However, the diameter of the Au plasmons is different for different deposition durations. The diameter of Au plasmons is estimated to be  $\sim 115$  nm, 129 nm, 140 nm, and 171 nm for deposition times 30, 45, 60, and 75 s, respectively. Since Au plasmons are distributed over the photoanodes surface, Au plasmons dispersion leads to a plasmon active surface. The presence of plasmons is solely responsible for the thermal effects. There is a difference between the actual temperature ( $T_A$ ) and the measured temperature ( $T_M$ ) of the synthesized ZnO nanorod photoanodes. The reaction rate, according to Arrhenius theory, is given as,

$$R \propto \exp(-E_a/k_B T) \tag{1}$$

where  $E_a$  is the activation energy and  $k_B$  is the Boltzmann constant. If  $T_M$  is less than the  $T_A$  of the photoanode, it appears that the reaction rates overshoot the Arrhenius law [10]. A simple correlation between the photoanode temperature,  $T_M$ , and the

incident illumination intensity  $I_{inc}$ , is given as follows:

$$T_A = T_{dark} + a I_{inc} = T_M + a I_{inc} \tag{2}$$

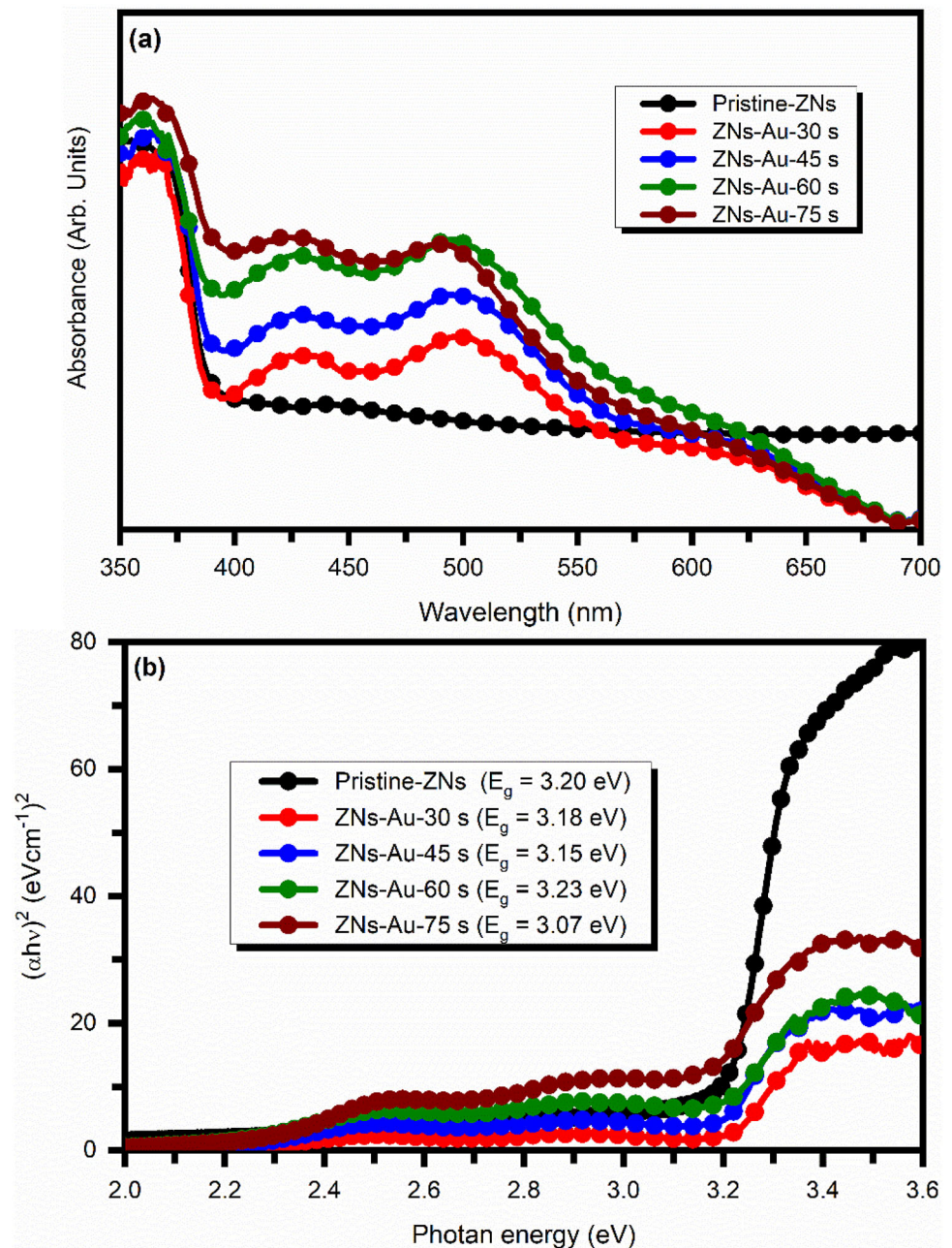
where  $T_{dark}$  is reactor temperature in the dark and 'a' is the photothermal conversion coefficient, which depends on several parameters such as material density number, illumination wavelength, size, and plasmonic material. Due to illumination, the slow heating effect can be easily incorporated by including a non-linear term  $I_{inc}$  with temperature [10].

### 3.3 UV-visible spectroscopy analysis

UV-Visible spectra were recorded to get the range of light absorption and Au plasmon's effect on the top of ZNs photoanodes. Figure 4 shows the absorption spectra and Tauc plots of all synthesized photoanodes.

As seen, the absorption range of photoanodes changes with respect to Au plasmon's deposition duration (Fig. 4a). As the deposition duration of Au

**Fig. 4** **a** UV–Visible absorption spectra for pristine-ZNs, ZNs-Au-30 s, ZNs-Au-45 s, ZNs-Au-60 s, and ZNs-Au-75 s and **b** Tauc plot used to estimate the band gap



plasmons increases, the absorption ranges increase in the visible region. The hot electrons induce the interaction between light and Au plasmons. The pristine-ZNs photoanode exhibits an absorption edge at  $\sim 370$  nm. The Tauc plot (Fig. 4b) defines its band edge position as  $\sim 3.2$  eV. It means only the photons with energy greater than this value can be absorbed, corresponding to wavelengths less than 387 nm. As the Au plasmons contribute to the absorption of light,

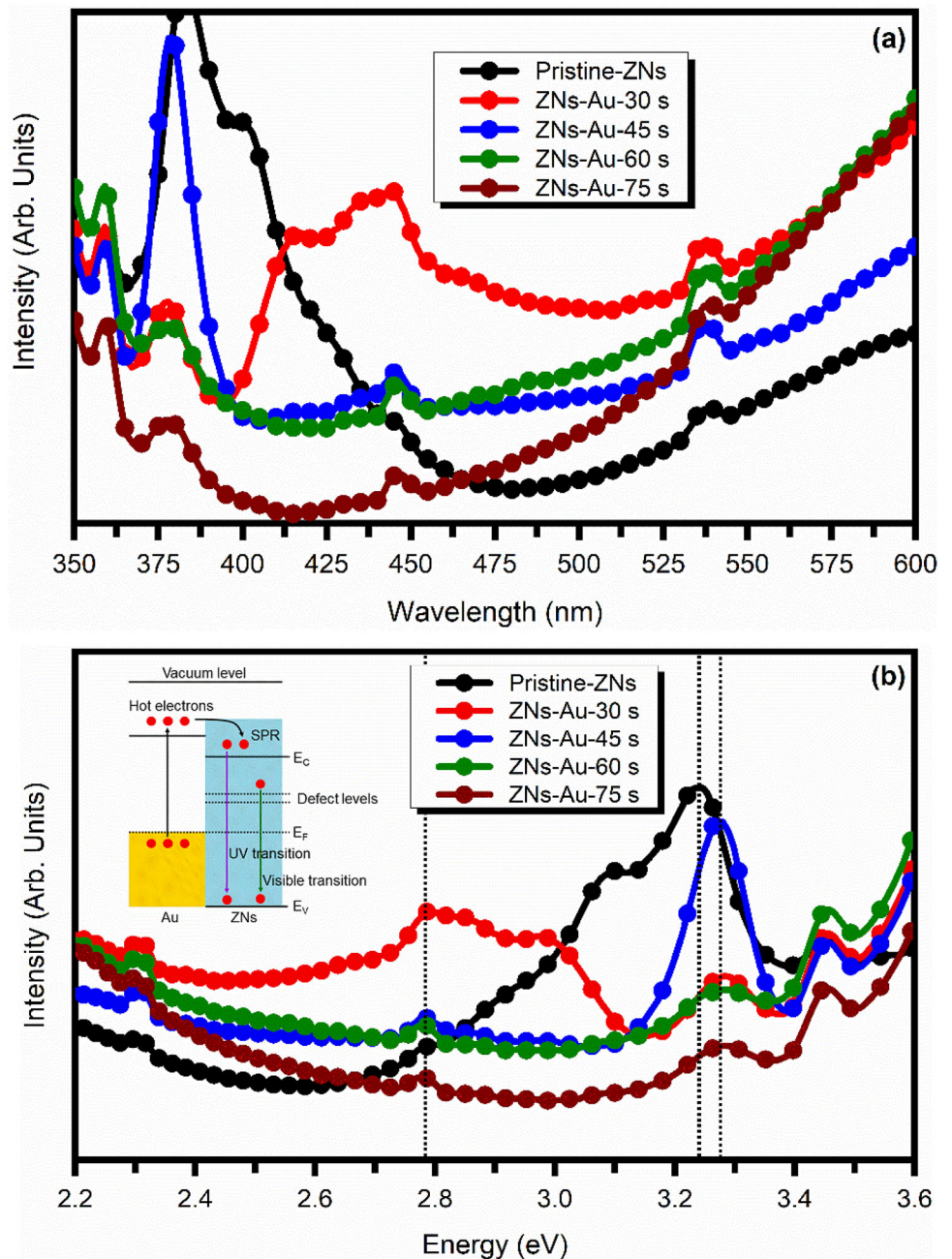
this rate varies remarkably. For example, the ZNs photoanode with Au plasmons for 30 s deposition time (ZRs-Au-30 s) exhibits an absorption range less than  $\sim 390$  nm, which corresponds to  $\sim 3.12$  eV. It indicates that the band edge position is decreased in ZRs-Au photoanode, resulting in an enhanced absorption range toward the visible region. Similarly, the band edge positions for ZNs-Au-45, 60, 75 s are obtained at  $\sim 3.152$ , 3.13, and 3.07 eV.

### 3.4 Photoluminescence spectroscopy analysis

The photoluminescence (PL) spectroscopy analysis further confirms results obtained from UV–Visible spectroscopy. By measuring the luminescence spectrum, it is possible to observe material imperfections and impurities. Figure 5 shows the PL spectrum of all synthesized photoanodes. The laser beam with a wavelength of 350 nm was used as an excitation wavelength. Figure 5a shows the emission spectra of

all synthesized photoanodes as a function of wavelength. Figure 5b shows emission spectra as a function of energy, and the inset shows the schematic defect band diagram for the ZNs-Au system. For pristine-ZNs photoanode, a strong emission characteristic of the excitonic band is observed in the UV region, and a small amount in the visible region, which are centered at 359 nm, 382 nm, 402 nm, and 538 nm corresponding to energy 3.45 eV, 3.23 eV, 3.08 eV, and 2.31 eV, respectively. The highest peak

**Fig. 5** PL spectra for pristine-ZNs, ZNs-Au-30 s, ZNs-Au-45 s, ZNs-Au-60 s, and ZNs-Au-75 s **a** Emission spectra as a function of wavelength **b** Emission spectra as a function of energy. Inset shows the schematic of defect band diagram for the ZNs-Au system



is located at 3.23 eV, indicating strong emission in the UV region and describing the band gap transition. As plasmonic Au is attributed to the ZNs, it causes enhancement of PL properties and large separation of excited electron–hole pairs upon visible light excitation. As we observe in Fig. 5a, the synthesized photoanodes exhibit a broad emission band in the visible region. The largest emission is concentrated for ZNs-Au-30 s. It shows a good peak at 443 nm with high intensity and two peaks with low intensity comparably at 415 nm and 537 nm in the visible region. The peak at 537 nm still has high intensity than the peak at 537 nm of pristine-ZNs photoanode. On the other hand, the central emission peaks of ZNs-Au describes the emission of band gap transition and higher electron–hole recombination between the conduction band and the sublevel, which is created in the band gap due to Au plasmons. Consequently, the excitonic emission band is shifted in Au plasmons from the UV region to the visible region.

The visible emission intensity of ZNs-Au was drastically decreased compared to pristine-ZNs implying that the incorporation of plasmonic Au onto ZNs probably quenches the defect-related emission effect of ZnO nanorods in the visible range. We think that the incorporation of plasmonic Au in ZNs may inject hot electrons into the conduction band of ZNs, which result in quenching of visible emission. Recently Nguyen et al. [41] and Do et al. [42] have observed quenching of visible emission Au-decorated ZnO structures for photocatalytic and gas sensing devices.

### 3.5 Photoelectrochemical (PEC) properties

J-V characteristics, EIS, and MS analysis were carried out to understand the PEC performance of the synthesized photoanodes. The PEC activity for all the synthesized photoanodes was recorded by linear sweep voltammetry (LSV) using three-electrode cells in the range 1.0 to 1.0 V versus SCE in the 0.5 M  $\text{N}_2\text{SO}_4$  electrolyte. The result is shown in Fig. 6a. The current was recorded in the dark in the first step, but a small current density was still observed. This current can be due to a non-faradic reaction. In the second step, the photoelectrode was illuminated by light, and a large amount of current was observed. Upon illumination, the photoelectrodes exhibit a direct photoexcitation, which leads to the generation of electron–hole pairs. Electrons migrate toward Pt

(counter electrode), where  $\text{H}_2$  would be produced by reducing protons. The holes react with water molecules to evolve  $\text{O}_2$ .

Photo-current density for pristine-ZNs at 1.0 V/SCE under the illumination is around  $324 \mu\text{A}/\text{cm}^2$  and for ZNs-Au-30 s, ZNs-Au-45 s, ZNs-Au-60 s, ZNs-Au-75 s are  $420 \mu\text{A}/\text{cm}^2$ ,  $540 \mu\text{A}/\text{cm}^2$ ,  $660 \mu\text{A}/\text{cm}^2$ , and  $581 \mu\text{A}/\text{cm}^2$  respectively. The synthesized photoanodes with Au plasmons exhibit more photo-current density than the pristine photoanode. The plasmonic layer of Au increases the photo-current density since the confined plasmonic effect of Au clusters present on the top of ZNs helps to enhance localized field strength, leading to an increase in the light absorption coefficient.

According to the investigation, Au plasmons absorb light and evolve hot electrons. These hot electrons insert in the conduction band of ZnO and further drift toward the cathode, leading to enhancement in the photo-current density (see schematic in Fig. 5b inset). As the concentration of Au plasmons is increased to a specific limit on ZNs surface, the photo-current density is increased. Nevertheless, when it exceeds the limit, the photo-current density is decreased. For instance, the ZNs-Au-75 s exhibits less photo-current density than ZNs-Au-60 s. The high photo-current density is obtained from ZNs-Au-60 s, which is around  $660 \mu\text{A}/\text{cm}^2$ . PCE of photoanodes has been calculated using [43],

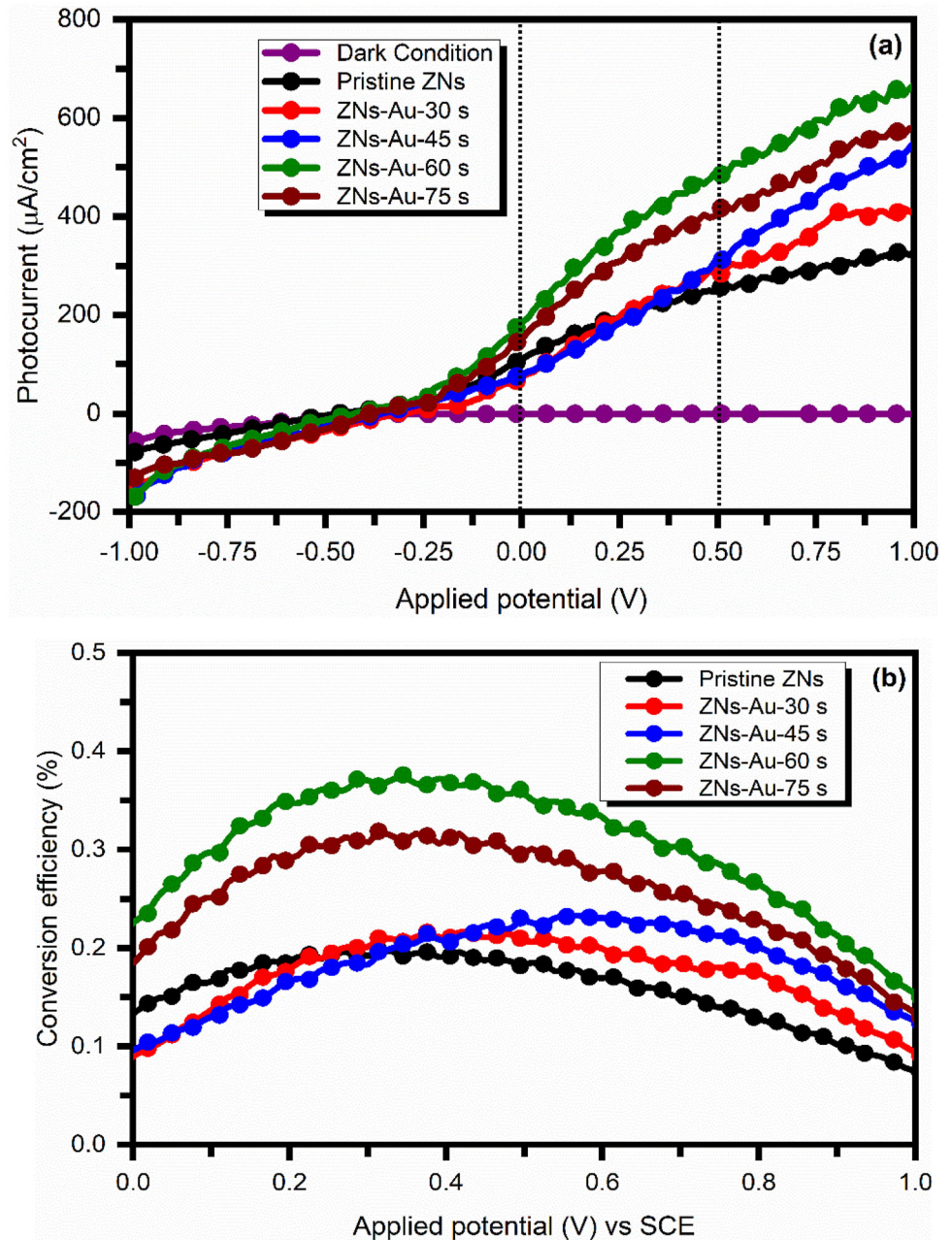
$$PCE = \frac{J_{\text{Ph}} \times (1.23 - |V_{\text{Bias}}|)}{P_{\text{Light}}} \quad (3)$$

where  $J_{\text{Ph}}$  is the photo-current density,  $V_{\text{Bias}}$  is applied voltage between photoanode and counter electrode, and  $P_{\text{Light}}$  is the power density of incident light ( $100 \text{ mW}/\text{cm}^2$ ). Figure 6b shows the photo-conversion efficiency of photoanodes for Au plasmons loaded for different time durations. The maximum PCE is obtained for ZNs-Au-60 s (0.38%), whereas for pristine-ZNs, the PCE is  $\sim 0.20\%$ .

The *hot electron mechanism* can be used to explain two critical phenomena. Foremost, it explains the inherent capability of high-energy electrons tunneling to the adjacent semiconductor through the Schottky barrier. These electrons can be used for photodetection at frequencies lower than the band-gap of the semiconductor. Secondly, noble metals, which are generally considered bad catalysts, contribute immensely to catalysis reactions when subjected to visible electromagnetic radiation. Plasmons



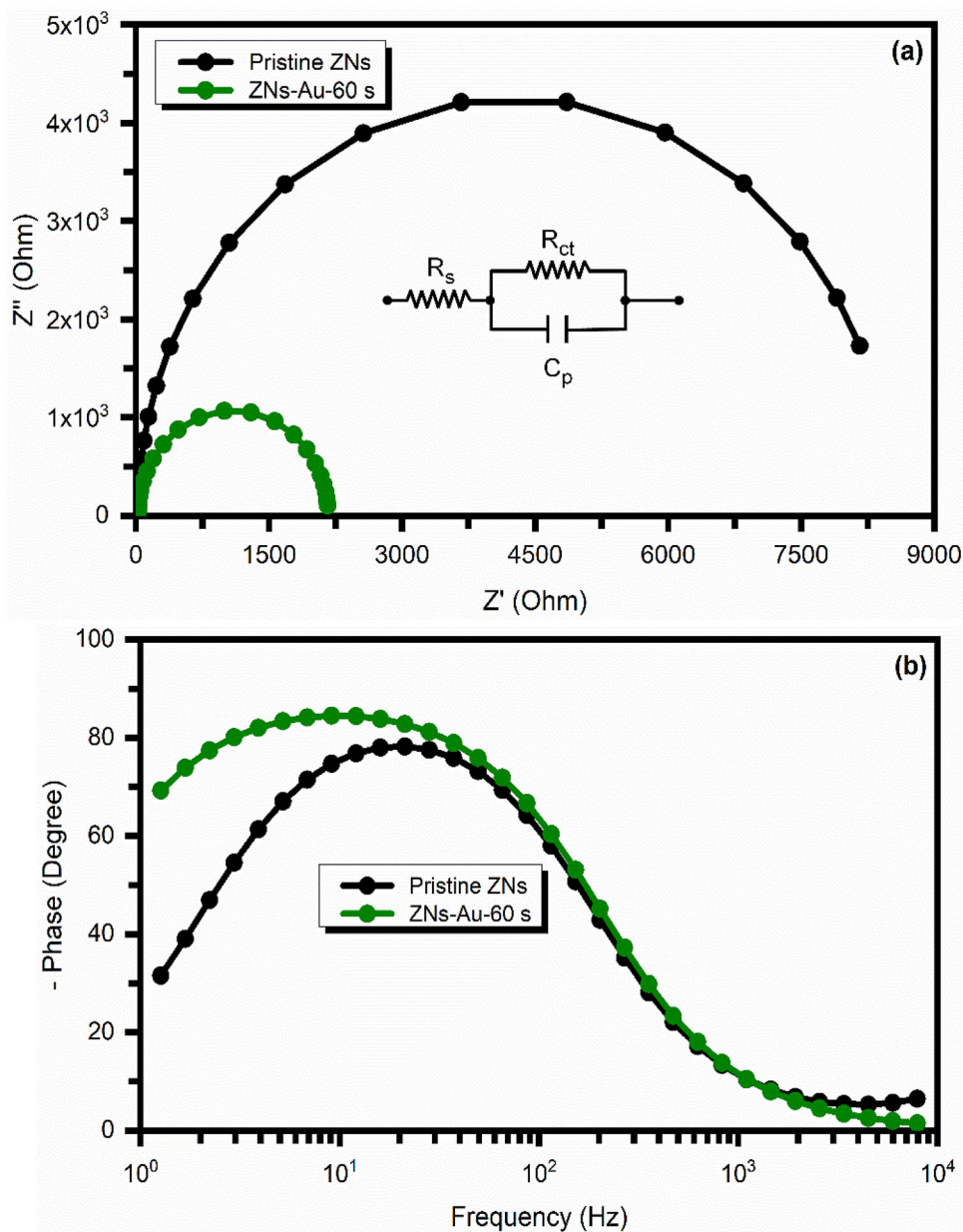
**Fig. 6** PEC characteristics of synthesized photoanodes: **a** J-V characteristics and **b** Photo-conversion efficiency



provide energy pathways with low activation to electrons. The presence of *hot electrons* helps to reduce activation energy and provides favorable reaction pathways as a function of number density. Loading of plasmons helps in circumventing the well-known limitation associated with photocatalysis occurring at high temperatures. EIS is an experimental technique that determines the dielectric properties of synthesized photoanodes and measures their impedance over a series of frequencies. The corresponding Nyquist and Bode plots are shown in Fig. 7. The arc

diameters typically represent the effective dissociation of photo-generated electron-hole pairs and their prolonged lifetime. The smaller arc diameter of ZNs-Au photoanodes describes the prolonged lifetime of photo-generated charge carriers compared to the bare-ZNs photoanodes (Fig. 7a). The inset of Fig. 7a shows the equivalent circuit model used to measure the electrical parameters such as solution resistance ( $R_s$ ), charge transfer resistance ( $R_{ct}$ ), and capacitance ( $C_p$ ).

**Fig. 7** **a** Nyquist plot for pristine-ZNs and ZNs-Au-60 s photoanodes at 0.5 V under illumination in 0.5 M Na<sub>2</sub>SO<sub>4</sub>, **b** Bode plot of pristine-ZNs and ZNs-Au-60 s at a bias potential of 0.5 V in light



As the Au plasmons layer takes part in the operation, it promotes the transfer of electrons within the semiconductor and restrains the electron/hole recombination. The lifetime of charge carriers in the photoanodes has been estimated using [44],

$$\tau = \frac{1}{2\pi f_{\max}} \quad (4)$$

where  $f_{\max}$  is the frequency at the maximum phase angle in the Bode plot (Fig. 7b).

The lifetimes of photoelectrons for the bare-ZNs and ZNs-Au-60 s photoanodes are obtained 123 ms and 170 ms, respectively. Therefore, the most

extended lifetime is predicted for ZNs-Au-60 s photoanode. To investigate the core mechanism involved in embedded plasmonic configuration and properties such as flat band potential (built-in potential), doping density, and Helmholtz capacitance, MS was studied. Figure 8 shows the MS plot from which capacitance was calculated and is used to estimate the density of charge carriers using [45],

$$\frac{1}{C^2} = \left( \frac{2}{e\epsilon_0\epsilon_r N_D A^2} \right) \left( V - V_{FB} - \frac{KT}{e} \right) \quad (5)$$

where  $C$  is the capacitance of the space charge region of the film at potential  $V$ ,  $V_{FB}$  is flat band potential,  $\epsilon_r$

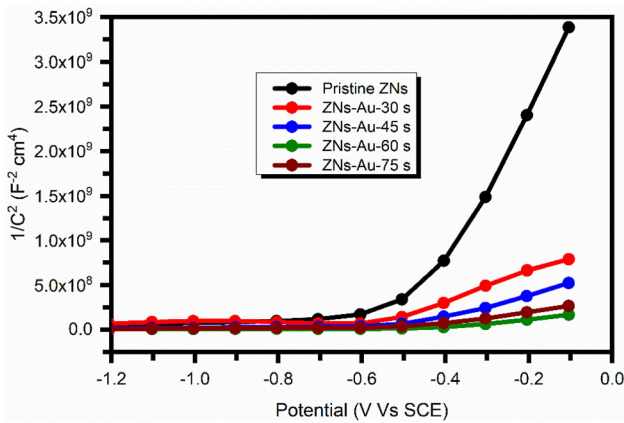


**Fig. 8** Mott-Schottky plots for ZNs-bare, ZNs-Au-30 s, ZNs-Au-45 s, ZNs-Au-60 s, and ZNs-Au-75 s photoanodes

is a dielectric constant which is  $\sim 8$  for bulk ZnO,  $N_D$  is free carrier concentration,  $K$  is the Boltzmann constant, and  $T$  is the absolute temperature.

The free charge carrier concentration can be given as follows[46]:

$$N_D = \frac{2}{e\epsilon_0\epsilon_r A^2 (\text{Slope})} \tag{6}$$

All the synthesized photoanodes exhibited positive slopes, depicting the n-type nature of ZnO photoanodes. In the given plot, the slope is used to determine the doping density ( $N_d$ ), and intercepts with the  $x$ -axis define the flat band potential ( $V_{FB}$ ). The flat band potential can be calculated from the intercept of the plot as [46],

$$V_{FB} = - \left[ \frac{(\text{Intercept})}{(\text{Slope})} + \frac{KT}{e} \right] \tag{7}$$

where  $kT/e$  is a correction factor  $\sim 0.025$  V that does not affect  $V_{fb}$  and intercept with slope can be defined from the plot after the linear fitting. The  $N_d$  for ZNs photoanode is around  $2.0 \times 10^{21}/\text{cm}^3$ , which has increased for ZNs with the incorporation of Au plasmons, as shown in Table 1. The ZNs-Au

photoanodes exhibit more donor density than the pristine-ZNs. At an applied potential 1.0 V, the calculated space charge layers were 0.80 nm for pristine-ZNs and 0.21 nm for ZNs-Au-75 s. The efficient charge separation transport and enhancement of PEC performance can be interpreted by charge carrier density. The enhancement in the carrier density confirms the efficiency of these two factors. It should be noted that these carrier densities were obtained based on the surface area of photoanodes exposed to the electrolyte. A positive shift is observed in flat band potential, suggesting a decrease in the binding band edge. Hence, donor density and bulk charge transport properties were improved via Au plasmons incorporation in ZNs.

### 4 Conclusion

We have successfully synthesized Au-dispersed ZNs-based photoanodes by the two-step PEC deposition method. The results indicate that the plasmonic layer of Au enhances the light absorption properties of synthesized photoanodes. All ZNs-Au photoanodes exhibited enhanced PEC response compared to pristine-ZNs. The ZNs-Au-60 s had shown the highest photo-current density ( $\sim 660 \mu\text{A}/\text{cm}^2$  at a bias of 1.0 V/SCE) than all synthesized photoanodes. The acquired PEC efficiency of ZNs-Au-60 s photoanode under light illumination was 0.38%, which is 1.9 times PEC efficiency for pristine-ZNs. We believe that the increased absorption in the visible region due to the surface plasmon resonance effect and the decreased photo-generated electron–hole recombination lead to a remarkably enhanced PEC performance. The UV–Visible spectroscopy analysis revealed that the ZNs-Au-60 s photoanode has a good absorption band in the visible region. The band gap values shifted toward the visible region from 3.20 to 3.07 eV for pristine-ZNs and ZNs-Au-60 s

**Table 1** Flat band potential ( $V_{fb}$ ), donor density ( $N_d$ ), and depletion layer width ( $W$ ) of synthesized photoanodes at 1.0 V

Samples	Flat band potential (V vs. RHE)	Donor density( $\text{cm}^{-3}$ )	Depletion layer width (nm)
ZNs-Pristine	− 0.48	$2.00 \times 10^{21}$	0.80
ZNs-Au-30 s	− 0.58	$1.08 \times 10^{22}$	0.36
ZNs-Au-45 s	− 0.54	$1.40 \times 10^{22}$	0.31
ZNs-Au-60 s	− 0.50	$3.74 \times 10^{22}$	0.18
ZNs-Au-75 s	− 0.55	$3.03 \times 10^{22}$	0.21

photoanodes. EIS described that photoelectron lifetime in the ZNs-Au-60 s photoanode (170 ms) is remarkably more than pristine-ZNs (123 ms). The obtained results provide a straightforward and effective method for constructing and designing Au plasmons-embedded ZNs-based photoanodes with high PEC performance.

## Acknowledgements

Vidhika Sharma, Mohit Prasad, and Sandesh Jadkar are thankful to Indo-French Centre for the Promotion of Advanced Research-CEFIPRA, Department of Science and Technology, New Delhi, for special financial support. Sandesh Jadkar is also thankful to UGC for financial support under the UPE program. Vidya Doiphode, Ashvini Punde, Pratibha Shinde, Yogesh Hase, and Ashish Waghmare are thankful to the Ministry of New and Renewable Energy, Government of India for financial support under the National Renewable Energy Fellowship (NREF) program.

## References

1. D.G. Nocera, The artificial leaf. *Acc. Chem. Res.* **45**(5), 767–776 (2012)
2. Y. Tachibana, L. Vayssieres, J.R. Durrant, Artificial photosynthesis for solar water-splitting. *Nat. Photon* **6**, 511–518 (2012)
3. I. Dincer, C. Acar, Review and evaluation of hydrogen production methods for better sustainability. *Int. J. Hydrog. Energy* **40**(34), 11094–11111 (2015)
4. C. Acar, I. Dincer, Experimental investigation and analysis of a hybrid photoelectrochemical hydrogen production system. *Int. J. Hydrog. Energy* **39**(28), 15362–15372 (2014)
5. Z. Li, W. Luo, M. Zhang, J. Feng, Z. Zou, Photoelectrochemical cells for solar hydrogen production: current state of promising photoelectrodes, methods to improve their properties and outlook. *Energy Environ. Sci.* **6**, 347–370 (2013)
6. T. Bak, J. Nowotny, M. Rekas, C.C. Sorrell, Photo-electrochemical hydrogen generation from water using solar energy Materials-related aspects. *Int. J. Hydrog. Energy* **27**, 991–1022 (2002)
7. X. Chen, S. Shen, L. Guo, S.S. Mao, Semiconductor-based photocatalytic hydrogen generation. *Chem. Rev.* **110**, 6503–6570 (2010)
8. Z. Chen, H. Dinh, E. Miller, *Photoelectrochemical Water Splitting: Standards, Experimental, Methods and Protocols* (Springer, New York, 2013)
9. M. Prasad, V. Sharma, A. Rokade, S. Jadkar, Photoelectrochemical cell: a versatile device for sustainable hydrogen production. *Photoelectrochem. Sol Cells* **30**, 59–119 (2018)
10. Y. Sivan, Y. Dubi, Recent developments in plasmon-assisted photocatalysis-A personal perspective. *Appl. Phys. Lett.* **117**, 130501 (2020)
11. W. Hou, S.B. Cronin, A review of surface plasmon resonance-enhanced photocatalysis. *Adv. Funct. Mater.* **23**, 1612–1619 (2013)
12. M. Rycenga, C.M. Cobley, J. Zeng, W. Li, C.H. Moran, Q. Zhang, D. Qin, Y. Xia, Controlling the synthesis and assembly of silver nanostructures for plasmonic applications. *Chem. Rev.* **111**, 3669–3712 (2011)
13. F. Wu, X. Hu, J. Fan, E. Liu, T. Sun, L. Kang, W. Hou, C. Zhu, H. Liu, Photocatalytic activity of Ag/TiO<sub>2</sub> nanotube arrays enhanced by surface plasmon resonance and application in hydrogen evolution by water splitting. *Plasmonics* **8**(2), 501–508 (2013)
14. J. Lee, S. Mubeen, X. Ji, G.D. Stucky, M. Moskovits, Plasmonic photoanodes for solar water splitting with visible light. *Nano Lett.* **12**, 5014–5019 (2012)
15. Y. Wei, L. Ke, J. Kong, H. Liu, H. Jiao, X. Lu, H. Du, X.W. Sun, Enhanced photoelectrochemical water-splitting effect with a bent ZnO nanorod photoanode decorated with Ag nanoparticles. *Nanotechnology* **23**, 235401–235409 (2012)
16. X. Zhang, Y. Liu, Z. Kang, 3D branched ZnO nanowire arrays decorated with plasmonic Au nanoparticles for high-performance photoelectrochemical water splitting. *Appl. Mater. Interfaces* **6**, 4480–4489 (2014)
17. J. Li, S.K. Cushing, P. Zheng, F. Meng, D. Chu, N. Wu, Plasmon-induced photonic and energy-transfer enhancement of solar water splitting by a hematite nanorod array. *Nat. Commun.* **4**, 2651–2659 (2013)
18. I. Zhang, C.Y. Lin, V.K. Valev, E. Reisner, U. Steiner, J.J. Baumberg, Plasmonic enhancement in BiVO<sub>4</sub> photonic crystals for efficient water splitting. *Small* **10**, 3970–3978 (2014)
19. Z. Yin, B. Chen, M. Bosman, X. Cao, J. Chen, B. Zheng, H. Zhang, Au nanoparticle-modified MoS<sub>2</sub> nanosheet-based photoelectrochemical cells for water splitting. *Small* **10**, 3537–3543 (2014)
20. A. Sheikh, A. Yengantiwar, M. Deo, S. Kelkar, S. Ogale, Near-field plasmonic functionalization of light harvesting oxide-oxide heterojunctions for efficient solar photoelectrochemical water splitting: the AuNP/ZnFe<sub>2</sub>O<sub>4</sub>/ZnO system. *Small* **9**, 2091–2096 (2013)

21. Y. Zhong, K. Ueno, Y. Mori, X. Shi, T. Oshikiri, K. Murakoshi, H. Inoue, H. Misawa, Plasmon-assisted water splitting using two sides of the same SrTiO<sub>3</sub> single-crystal substrate: conversion of visible light to chemical energy. *Angew Chem. Int. Ed.* **53**, 10350–10354 (2014)
22. W.T. Kung, Y.H. Pai, Y.K. Hsu, C.H. Lin, C.M. Wang, Surface plasmon assisted Cu<sub>x</sub>O photocatalyst for pure water splitting. *Opt. Express* **21**, A221–A228 (2013)
23. X. Yang, A. Wolcott, G. Wang, A. Sobo, R.C. Fitzmorris, F. Qian, J.Z. Zhang, Y. Li, Nitrogen-doped ZnO nanowire arrays for photoelectrochemical water splitting. *Nano Lett.* **9**, 2331–2336 (2009)
24. M. Gupta, V. Sharma, J. Shrivastava, A. Solanki, A.P. Singh, V.R. Satsangi, S. Dass, R. Shrivastav, Preparation and characterization of nanostructured ZnO thin films for photoelectrochemical splitting of water. *Bull. Mater. Sci.* **32**, 23–30 (2009)
25. J. Han, Z. Liu, K. Guo, B. Wang, X. Zhang, T. Hong, High-efficiency photoelectrochemical electrodes based on ZnIn<sub>2</sub>S<sub>4</sub> sensitized ZnO nanotube arrays. *Appl. Catal. B* **163**, 179–188 (2015)
26. T. Hong, Z. Liu, H. Liu, L. Junqi, X. Zhang, J. Han, K. Guo, B. Wang, Preparation and enhanced photoelectrochemical performance of selenite-sensitized zinc oxide core/shell composite structure. *J. Mater. Chem. A* **3**, 4239–4247 (2015)
27. L. Yan, W. Zhao, Z. Liu, 1D ZnO/BiVO<sub>4</sub> heterojunction photoanodes for efficient photoelectrochemical water splitting. *Dalton Trans* **45**, 11346–11352 (2016)
28. A. Janotti, C.G.V. Walle, Fundamentals of zinc oxide as a semiconductor. *Rep. Prog. Phys.* **72**, 126501–126529 (2009)
29. Z.L. Wang, Zinc oxide nanostructures: growth, properties and applications. *J. Phys. Condens. Matter.* **16**, R829–R858 (2004)
30. V. Sharma, P. Kumar, J. Shrivastava, A. Solanki, V.R. Satsangi, S. Dass, R. Shrivastav, Vertically aligned nanocrystalline Cu-ZnO thin films for photoelectrochemical splitting of water. *J. Mater. Sci.* **46**, 3792–3801 (2011)
31. V. Sharma, P. Kumar, N. Singh, S. Upadhyay, V.R. Satsangi, S. Dass, R. Shrivastav, Photoelectrochemical water splitting with nanocrystalline Zn<sub>1-x</sub>Ru<sub>x</sub>O thin films. *Int. J. Hydrog. Energy* **37**, 12138–12149 (2012)
32. V. Sharma, M. Dixit, V.R. Satsangi, S. Dass, S. Pal, R. Shrivastav, Photoelectrochemical splitting of water with nanocrystalline Zn<sub>1-x</sub>Mn<sub>x</sub>O thin films: first-Principle DFT computations supporting the systematic experimental endeavor. *Int. J. Hydrog. Energy* **39**, 3637–3648 (2014)
33. V. Sharma, M. Prasad, S. Jadkar, S. Pal, Influence of carbon and phosphorus doping on electronic properties of ZnO. *J. Mater. Sci. Mater. Electron.* **27**(12), 12318–12322 (2013)
34. Y. Liu, Y. Gu, X. Yan, Z. Kang, S. Lu, Y. Sun, Y. Zhang, Design of sandwich-structured ZnO/ZnS/Au photoanode for enhanced efficiency of photoelectrochemical water splitting. *Nano Res.* **8**, 2891–2900 (2015)
35. S.M. Lam, J.A. Quek, J.C. Sin, Mechanistic investigation of visible light responsive Ag/ZnO micro/nanoflowers for enhanced photocatalytic performance and antibacterial activity. *J. Photochem. Photobiol., A* **353**, 171–184 (2018)
36. R.B. Wei, P.Y. Kuang, H. Cheng, Y.B. Chen, J.Y. Long, M.Y. Zhang, Z.Q. Liu, Plasmon-enhanced photoelectrochemical water splitting on gold nanoparticle decorated ZnO/CdS nanotube arrays. *ACS Sustain. Chem. Eng.* **5**(5), 4249–4257 (2017)
37. T. Wang, R. Lv, P. Zhang, C. Li, J. Gong, Au nanoparticle sensitized ZnO nanopencil arrays for photoelectrochemical water splitting. *Nanoscale* **7**, 77–81 (2015)
38. B. Kumari, S. Sharma, V.R. Satsangi, S. Dass, R. Shrivastav, Surface deposition of Ag and Au nano-isles on ZnO thin films yields enhanced photoelectrochemical splitting of water. *J. Appl. Electrochem.* **45**, 299–312 (2015)
39. M. Uddin, M. Alam, A. Asiri, M. Rahman, T. Toupance, M. Islam, A novel highly selective electrochemical chlorobenzene sensor based on ternary oxide RuO<sub>2</sub>/ZnO/TiO<sub>2</sub> nanocomposites. *RSC Adv.* **10**, 122–132 (2020)
40. Y. Liu, X. Yan, Z. Kang, Y. Li, Y. Shen, Y. Sun, L. Wang, Y. Zhang, Synergistic effect of surface plasmonic particles and surface passivation layer on ZnO nanorods array for improved photoelectrochemical water splitting. *Sci. Rep.* **6**, 29907 (2016)
41. T.H. Nguyen, T.A. Do, H.T. Giang, T.G. Ho, Q.N. Pham, M.T. Man, Effect of metal-support couplings on the photocatalytic performance of Au-decorated ZnO nanorods. *J. Mater. Sci.: Mater. Electron.* **31**, 14946–14952 (2020)
42. T. Do, T.G. Ho, T.H. Bui, Q.N. Pham, H.T. Giang, T.T. Do, D.V. Nguyen, D.L. Tran, Surface-plasmon-enhanced ultraviolet emission of Au-decorated ZnO structures for gas sensing and photocatalytic devices. *Beilstein J. Nanotechnol.* **9**, 771–779 (2018)
43. D. Rekha, L.R. Baby, K.H. Gyu, P.H. Borse, Enhanced solar photoelectrochemical conversion efficiency of ZnO: Cu electrodes for water-splitting application. *Int. J. Photoenergy* (2013). <https://doi.org/10.1155/2013/928321>
44. J. Lin, Y.U. Heo, A. Nattestad, Z. Sun, L. Wang, J.H. Kim, S.X. Dou, 3D Hierarchical rutile TiO<sub>2</sub> and metal-free organic sensitizer producing dye-sensitized solar cells 8.6% conversion efficiency. *Sci. Rep.* **4**, 5769 (2014)
45. C. Windisch, G. Exarhos, Vac, Mott-Schottky analysis of thin ZnO films. *J. Sci. Technol.* **18**, 1677–1680 (2000)
46. B. Bera, A. Chakraborty, T. Kar, P. Leuaa, M. Neergat, Density of states, carrier concentration, and flat band potential

derived from electrochemical impedance measurements of N doped carbon and their influence on electrocatalysis of oxygen reduction reaction. *Phys. J. Chem. C.* **121**, 20850–20856 (2017)

**Publisher's Note** Springer Nature remains neutral with regard to jurisdictional claims in published maps and institutional affiliations.